Inorganic Chemistry
Article
pubs.acs.org/IC

A Series of Tetrathiafulvalene-Based Lanthanide Complexes Displaying Either Single Molecule Magnet or Luminescence—Direct Magnetic and Photo-Physical Correlations in the Ytterbium Analogue

Fabrice Pointillart,*,† Boris Le Guennic,† Thomas Cauchy,‡ Stéphane Golhen,† Olivier Cador,† Olivier Maury,§ and Lahcène Ouahab†

†Organométalliques: Matériaux et Catalyse, UMR 6226 CNRS-UR1 Institut des Sciences Chimiques de Rennes, Université de Rennes 1, 35042, Rennes Cedex, France

‡Laboratoire MOLTECH-Anjou, Université d'Angers CNRS-UMR 6200, 2 Bd Lavoisier 49045 Angers, France

§Laboratoire de Chimie de l'ENS-Lyon-UMR 5182 CNRS−ENS Lyon−Université de Lyon 1, 46 Allée d'Italie, 69364 Lyon Cedex 07, France

Supporting Information

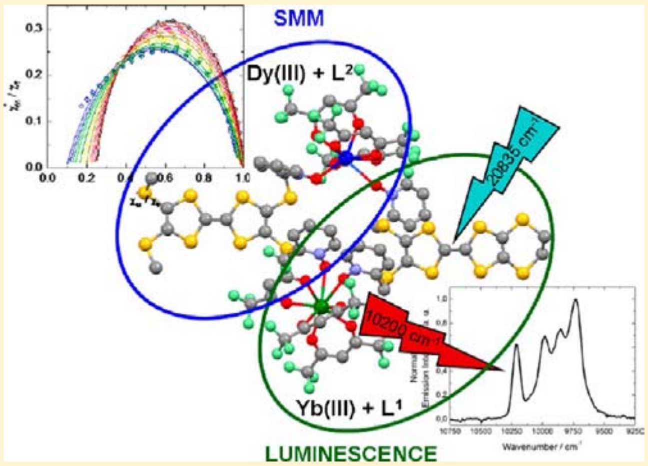

ABSTRACT: The reaction between (4,5-bis(2-pyridyl-*N*-oxidemethylthio)-4′,5′)-ethylenedithiotetrathiafulvene (L^1) or -methyldithiotetrathiafulvene (L^2) ligands and $Ln(hfac)_3 \cdot nH_2O$ precursors (Ln^{III} = Pr, Tb, Dy, Er, and Yb) leads to the formation of seven dinuclear complexes of formula $[Ln_2(hfac)_6(H_2O)_x(L^y)_2]$ ($x = 2$ and $y = 1$ for Ln^{III} = Pr (**1**); $x = 0$ and $y = 1$ for Ln^{III} = Tb (**2**), Dy (**3**), Er (**4**) and Yb (**5**); $x = 0$ and $y = 2$ for Ln^{III} = Tb (**6**) and Dy (**7**)). Their X-ray structures reveal that the coordination environment of each Ln^{III} center is filled by two *N*-oxide groups coming from two different ligands L^y. UV−visible absorption properties have been experimentally measured and rationalized by TD-DFT calculations. The temperature dependences of static magnetic measurements have been fitted. The ground state corresponds to the almost pure $|M_J = \pm 13/2\rangle$ while the first excited state ($\pm 0.77|\pm 11/2\rangle \pm 0.50|\pm 3/2\rangle \pm 0.39|\pm 5/2\rangle$) is located at 19 cm⁻¹ and 26.9 cm⁻¹ respectively for **3** and **7**. Upon irradiation at 77 K and at room temperature, in the range 25 000−20 835 cm⁻¹, both compounds **4** and **5** display a metal-centered luminescence attributed to $^4I_{13/2} \rightarrow {}^4I_{15/2}$ (6660 cm⁻¹) and $^2F_{5/2} \rightarrow {}^2F_{7/2}$ (9972 cm⁻¹) transitions, respectively. Emission spectroscopy provides a direct probe of the $|\pm 5/2\rangle$ ground state multiplet splitting, which has been confronted to magnetic data. The energy separation of 225 cm⁻¹ between the ground state and the first excited level ($M_J = \pm 3/2$) fits exactly the second emission line (234 cm⁻¹). While no out-phase-signal is detected for **3**, the change of ligand $L^1 \rightarrow L^2$ induces a change of coordination sphere symmetry around the Dy^{III} increasing the energy splitting between the ground and first excited states, and **7** displays a single molecule magnet behavior.

■ INTRODUCTION

The association of tetrathiafulvalene (TTF)-based ligands with 4f elements is a recent alternative way compared to the classical π−d approach for the elaboration of multifunctional materials[1] that extends the possible combination of physical properties to electronic conductivity, magnetism, and luminescence. Such π−f systems have been first elaborate using a "through space" strategy[2] or more recently a "through bond" approach.[3]

From an optical point of view, lanthanides possess specific luminescent properties, and their association with β-diketones has garnered a large amount of attention[4] due to their potential application in the design of chelate lasers,[5] efficient organic light-emitting diodes (OLEDs),[6] and polymer light-emitting diodes (PLEDs).[7]

They can also have application as NMR shift reagents[8] in analytical applications and as modern antibody catalysts in biochemistry.[9] In most of the studied examples, the unoccupied coordination positions are filled by organic ligands which play the role of antenna chromophores for the sensitization of the lanthanide emission. The near-infrared (NIR) luminescence of the Pr^{III}, Nd^{III}, Er^{III}, and Yb^{III} is more devoted to technological

Received: January 31, 2013
Published: May 9, 2013

Scheme 1. Representation of the Ligands L^1 and L^2

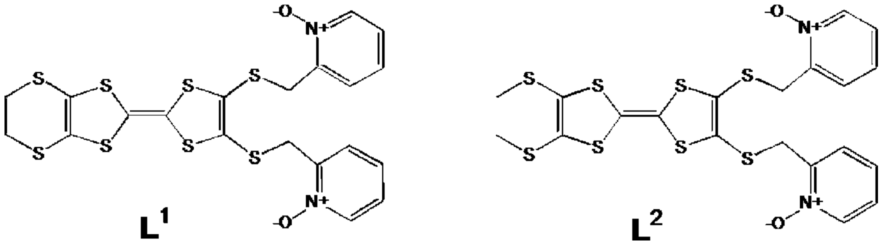

applications in areas ranging from medical imaging to optical communication.[10]

From a magnetic point of view, 4f ions present a large magnetic moment and a large anisotropy.[11] These advantages promote lanthanides as good candidates in the design of Single Molecule Magnets (SMMs)[12] all the more since lanthanide-based SMMs show better dynamic parameters than transition-metal-based ones.[13] Such behavior can also be observed for a magnetically isolated 4f ion; in this case, we talk about Single Ion Magnets (SIMs). The latter phenomenon is observed with axial electron density for Tb^{III}/Dy^{III}[14] ions or equatorial electron density for Er^{III}[15]/Yb^{III}[16] ions.[17]

In these lines, we report the functionalization of the two 4′,5′-ethylenedithiotetrathiafulvalene (EDT-TTF) and 4′,5′-methyldithiotetrathiafulvalene (BMT-TTF) cores with two 2-pyridyl-*N*-oxidemethylthio arms to guarantee the coordination with the lanthanide ions and to permit the sensitization of the NIR luminescence. The reaction between the 4,5-bis(2-pyridyl-*N*-oxidemethylthio)-4′,5′-ethylenedithiotetrathiafulvene (**L^1**; Scheme 1) or 4,5-bis(2-pyridyl-*N*-oxidemethylthio)-4′,5′-methyldithiotetrathiafulvene (**L^2**; Scheme 1) and the $Ln(hfac)_3 \cdot nH_2O$ precursors (where $hfac^-$ = 1,1,1,5,5,5-hexafluoroacetylacetonate anion and Ln = Pr^{III}, Tb^{III}, Dy^{III}, Er^{III}, and Yb^{III}) lead to the formation of seven dinuclear complexes of formula $[Ln_2(hfac)_6(H_2O)_x(L^y)_2]$ ($x = 2$ and $y = 1$ for Ln = Pr^{III} (**1**); $x = 0$ and $y = 1$ for Ln = Tb^{III} (**2**), Dy^{III} (**3**), Er^{III} (**4**) and Yb^{III} (**5**); $x = 0$ and $y = 2$ for Ln = Tb^{III} (**6**) and Dy^{III} (**7**)). The samples have been characterized by X-ray diffraction on single crystals, magnetic measurements, UV−visible absorption, and IR emission spectroscopy. In case of **L^1**, the optical properties have been rationalized by DFT and TD-DFT calculations. The influence of the nature of the EDT-TTF or BMT-TTF core on the crystal packing, arrangement of the arms, and so on the symmetry of the coordination sphere around the metal center is studied. In particular, we will correlate the consequences that the structural changes have on the magnetic and luminescence properties. Both properties were correlated in the case of **5**.

■ EXPERIMENTAL SECTION

General Procedures and Materials. All solvents were dried using standard procedures for the synthesis of **L^1** and **L^2**, while standard solvents were used for the reactions of coordination. The precursors $Ln(hfac)_3 \cdot xH_2O$ ($x = 3$ for Ln^{III} = Pr and $x = 2$ for Ln^{III} = Tb, Dy, Er, and Yb; $hfac^-$ = 1,1,1,5,5,5-hexafluoroacetylacetonate anion)[18] were synthesized following previously reported methods. All other reagents were purchased from Aldrich Co., Ltd. and used without further purification.

Crystallography. Single crystals of **1**−**5** were mounted on an APEXII Bruker-AXS diffractometer (Mo Kα radiation source, λ = 0.71073 Å, T = 150(2) K) while single crystals of **L^2**, **6**, and **7** were mounted on a Nonius four circle diffractometer equipped with a CCD camera and a graphite monochromated Mo Kα radiation source (λ = 0.71073 Å, T = 293(2) K) for data collection, from the Centre de Diffractométrie (CDIFX), Université de Rennes 1, France. The space groups were checked with the PLATON/ADDSYM program,[19a] and the structures were solved via direct methods using the SIR-97 program and refined with a full matrix least-squares method on F^2 using the SHELXL-97 program[19c] for **1** and **3** while only a cell determination was performed for **2**, **4**, and **5**. Despite all structures contain solvent accessible voids, no SQUEEZE procedure was performed. Crystallographic data are summarized in Table 1.

Physical Measurements. Elemental analyses of the **L^1**−**L^2** ligands and **1**−**7** compounds were performed at the Centre Régional de Mesures Physiques de l'Ouest, Rennes. ^1H NMR was recorded on a Bruker AC 400 spectrometer. Chemical shifts are reported in parts per million referenced to TMS for ^1H NMR. Absorption spectra were recorded on a Varian Cary 5000 UV−visible−NIR spectrometer equipped with an integration sphere. The luminescence spectra were measured using a Horiba-Jobin Yvon Fluorolog-3 spectrofluorimeter, equipped with a three slit double grating excitation and emission monochromator with dispersions of 2.1 nm/mm (1200 grooves/mm). The steady-state luminescence was excited by unpolarized light from a 450 W xenon CW lamp and detected at an angle of 90° for diluted solution measurements or at 22.5° for solid state measurement (front face detection) by a red-sensitive Hamamatsu R928 photomultiplier tube. Spectra were reference corrected for both the excitation source light intensity variation (lamp and grating) and the emission spectral response (detector and grating). Uncorrected near-infrared spectra were recorded at an angle of 45° using a liquid nitrogen cooled, solid indium/gallium/arsenic detector (850−1600 nm). The ac and dc magnetic susceptibility measurements were performed with ground single crystals pelletized in Teflon tape with a Quantum Design MPMS-XL SQUID magnetometer between 2 and 300 K in applied magnetic field of 0.2 T for temperatures of 2−20 K and 1 T for temperatures of 20−300 K. These measurements were all corrected for the diamagnetic contribution as calculated with Pascal's constants.

Computational Details. DFT geometry optimizations and TD-DFT excitation energy calculations of the ligand **L^1** were carried out with the Gaussian 09 (revision A.02) package[20] employing the PBE0 hybrid functional.[21] All atoms were described with the SVP basis sets.[22] The first 50 monoelectronic excitations were calculated for ligand **L^1**. In all steps, a modeling of bulk solvent effects (solvent = chloroform) was included through the Polarizable Continuum Model (PCM),[23] using a linear-response nonequilibrium approach for the TD-DFT step.[24] Molecular orbitals were sketched using the Gabedit graphical interface.[25]

Synthesis of 4,5-Bis(2-pyridyl-*N*-oxidemethylthio)-4′,5′-ethylenedithiotetrathiafulvene (L^1). A solution of 0.5 M EtONa/EtOH (14 mL) was added to a suspension of 4,5-bis(2′-cyanoethylthio)-4′,5′-ethylenedithiotetrathiafulvene[26] (0.640 g, 1.38 mmol) in anhydrous degassed EtOH (41 mL) under argon. After being stirred at room temperature for 4 h, the mixture was reacted with a solution of 2-(chloromethyl)pyridine-1-oxide[27] (0.593 g, 4.13 mmol) in anhydrous degassed EtOH (27 mL), and then the mixture was stirred for 16 h. H_2O (41 mL) was added to quench the reaction, and the mixture was poured into CH_2Cl_2 (345 mL), washed with saturated $NaHCO_3$ (3 × 55 mL), and water (210 mL). The organic extract was concentrated in a vacuum to give a red-brown oil which was purified by chromatography on alumina gel, initially with CH_2Cl_2 (to remove the unreacted alkyl halide) and then with CH_2Cl_2/MeOH (10:1) to

Table 1. X-Ray Crystallographic Data for the Ligand $(L^2)\cdot H_2O$ and the Complexes 1, 3, 6, and 7 and Cell Parameters for 2, 4, and 5

	$[Pr_2(hfac)_6(H_2O)_2(\mathbf{L^1})_2]$ (**1**)	$[Tb_2(hfac)_6(\mathbf{L^1})_2]$ (**2**)	$[Dy_2(hfac)_6(\mathbf{L^1})_2]$ (**3**)
formula	$C_{70}H_{42}Pr_2F_{36}N_4O_{18}S_{16}$	$C_{70}H_{38}Tb_2F_{36}N_4O_{16}S_{16}$	$C_{70}H_{38}Dy_2F_{36}N_4O_{16}S_{16}$
M/g mol^{-1}	2705.8	2705.8	2713.0
cryst syst	orthorhombic	monoclinic	monoclinic
space group	*Pnaa* (No. 56)		C2/*c* (No. 15)
cell params	$a = 20.3152(8)$ Å	$a = 38.0400(26)$ Å	$a = 38.2055(16)$ Å
	$b = 28.2622(10)$ Å	$b = 19.9480(15)$ Å	$b = 19.9095(7)$ Å
	$c = 39.7252(14)$ Å	$c = 37.8400(27)$ Å	$c = 37.6513(16)$ Å
		$\beta = 119.1290(14)°$	$\beta = 119.3738(19)°$
volume/Å^3	22808(2)	25082(8)	24958(2)
cell formula units	8		4
T/K	150 (2)	150(2)	150 (2)
diffraction refln	$1.76 \leq 2\theta \leq 55.02$		$2.38 \leq 2\theta \leq 54.90$
ρ_{calcd}, g cm^{-3}	1.576		1.444
μ, mm^{-1}	1.251		1.558
number of reflns	170135		99372
independent reflns	26176		28413
$F_o^2 > 2\sigma(F_o)^2$	14216		17610
number of variables	1315		1297
R_{int}, R_1, wR_2	0.1048, 0.0827, 0.2291		0.0589, 0.0688, 0.2063

	$[Er_2(hfac)_6(\mathbf{L^1})_2]$ (**4**)	$[Yb_2(hfac)_6(\mathbf{L^1})_2]$ (**5**)	$(\mathbf{L^2})\cdot H_2O$
formula	$C_{70}H_{38}Er_2F_{36}N_4O_{16}S_{16}$	$C_{70}H_{38}Yb_2F_{36}N_4O_{16}S_{16}$	$C_{20}H_{20}N_2O_3S_8$
M/g mol^{-1}	2720.5	2732.0	592
cryst syst	monoclinic	*monoclinic*	triclinic
space group			$P\bar{1}$ (No. 2)
cell params	$a = 37.9900(71)$ Å	$a = 37.7139(6)$ Å	$a = 8.3312(3)$ Å
	$b = 19.8700(41)$ Å	$b = 19.7700(2)$ Å	$b = 9.1008(2)$ Å
	$c = 38.2800(72)$ Å	$c = 38.1188(6)$ Å	$c = 17.5597(7)$ Å
	$\beta = 120.9700(19)°$	$\beta = 120.8612(3)°$	$\alpha = 82.012(2)°$
			$\beta = 80.795(2)°$
			$\gamma = 77.391(2)°$
volume/Å^3	24777(17)	24397(2)	1275.04(7)
cell formula units			2
T/K	150 (2)	150 (2)	293 (2)
diffraction refln			$2.36° \leq 2\theta \leq 66.42°$
ρ_{calc}, g.cm^{-3}			1.497
μ, mm^{-1}			0.722
number of reflns			13472
independent reflns			9644
$F_o^2 > 2\sigma(F_o)^2$			4629
number of variables			298
R_{int}, R_1, ωR_2			0.0314, 0.0699, 0.1926

	$[Tb(hfac)_3(\mathbf{L^2})]_2$ (**6**)	$[Dy(hfac)_3(\mathbf{L^2})]_2$ (**7**)
formula	$C_{70}H_{42}Tb_2F_{36}N_4O_{16}S_{16}$	$C_{70}H_{42}Dy_2F_{36}N_4O_{16}S_{16}$
M/g mol^{-1}	2710.0	2715.0
cryst syst	monoclinic	monoclinic
space group	$P2_1/n$ (No. 14)	$P2_1/n$ (No. 14)
cell parameters	$a = 11.9756(2)$ Å	$a = 11.9724(1)$ Å
	$b = 31.2646(8)$ Å	$b = 31.2383(4)$ Å
	$c = 13.7018(3)$ Å	$c = 13.7112(2)$ Å
	$\beta = 101.5144(12)°$	$\beta = 101.5104(6)°$
volume/Å^3	5026.9(2)	5024.8(1)
cell formula units	2	2
T/K	293 (2)	293 (2)
diffraction refln	$2.30° \leq 2\theta \leq 52.02°$	$2.60° \leq 2\theta \leq 55.78°$
ρ_{calc}, g cm^{-3}	1.790	1.796
μ, mm^{-1}	1.854	1.934
number of reflns	17596	65305
independent reflns	9837	11954
$F_o^2 > 2\sigma(F_o)^2$	6281	7307

Table 1. continued

	$[Tb(hfac)_3(\mathbf{L}^2)]_2$ (**6**)	$[Dy(hfac)_3(\mathbf{L}^2)]_2$ (**7**)
number of variables	714	761
R_{int}, R_1, ωR_2	0.0366, 0.0545, 0.1431	0.0668, 0.0521, 0.1360

give the pure desired ligand. Yield: 477 mg (61%). Anal. Calcd (%) for $C_{20}H_{16}N_2O_2S_8$: C, 41.96; H, 2.80; N, 4.90. Found: C, 42.23; H, 2.95; N, 4.80. ^{1}H NMR ($CDCl_3$): 8.29−8.27 (m, 4H), 7.35−7.24 (m, 4H), 4.13 (s, 4H), 3.32 (s, 4H).

Synthesis of 4,5-Bis(2-pyridyl-*N*-oxidemethylthio)-4′,5′-methyldithiotetrathiafulvene ($\mathbf{L}^2$). $\mathbf{L}^2$ is synthesized using a similar method to the one used for $\mathbf{L}^1$, but 4,5-bis(2′-cyano-ethylthio)-4′,5′-methyldithiotetrathiafulvene[26] is used instead of 4,5-bis(2′-cyano-ethylthio)-4′,5′-ethylenedithiotetrathiafulvene. Yield: 360 mg (46%). Orange single crystals suitable for X-ray study of $\mathbf{L}^2{\cdot}H_2O$ were obtained by slow evaporation of a saturated CH_2Cl_2/*n*-hexane (1:1 in volume) mixture of $\mathbf{L}^2$. Anal. Calcd (%) for $C_{20}H_{20}N_2O_3S_8$: C, 40.54; H, 3.38; N, 4.73. Found: C, 40.40; H, 3.49; N, 4.70. ($CDCl_3$): 8.17−8.11 (m, 4H), 7.25−7.12 (m, 4H), 3.36 (s, 4H), 2.37 (s, 6H).

Synthesis of Complexes 1−5. *$[Pr_2(hfac)_6(H_2O)_2(\mathbf{L}^1)_2]$ (**1**).* A total of 32.8 mg of $Pr(hfac)_3{\cdot}3H_2O$ (0.04 mmol) was dissolved in 5 mL of $CHCl_3$ and then added to a solution of 10 mL of $CHCl_3$ containing 22.9 mg of $\mathbf{L}^1$ (0.04 mmol). After 15 min of stirring, *n*-hexane was layered at 4 °C to give orange single crystals which are suitable for X-ray study. Yield: 42 mg (39%). Anal. Calcd (%) for $C_{70}H_{42}Pr_2F_{36}N_4O_{18}S_{16}$: C, 31.07; H, 1.55; N, 2.07. Found: C, 30.81; H, 1.64; N, 2.09.

*$[Ln_2(hfac)_6(\mathbf{L}^1)_2]$ (Ln = Tb (**2**), Dy (**3**), Er (**4**), and Yb (**5**)).* A total of 0.04 mmol of $Ln(hfac)_3{\cdot}2H_2O$ was dissolved in 5 mL of $CHCl_3$ and then added to a solution of 10 mL of $CHCl_3$ containing 22.9 mg of $\mathbf{L}^1$ (0.04 mmol). After 15 min of stirring, *n*-hexane was layered at room temperature to give yellow single crystals which are suitable for X-ray studies. Yield: 51 mg (47%), 55 mg (51%), 78 mg (72%), and 44 mg (40%), respectively, for compounds **2**−**5**. Anal. Calcd (%) for $C_{70}H_{38}Tb_2F_{36}N_4O_{16}S_{16}$: C, 31.07; H, 1.41; N, 2.07. Found: C, 31.31; H, 1.49; N, 2.00. Anal. Calcd (%) for $C_{70}H_{38}Dy_2F_{36}N_4O_{16}S_{16}$: C, 30.98; H, 1.40; N, 2.07. Found: C, 31.04; H, 1.41; N, 2.10. Anal. Calcd (%) for $C_{70}H_{38}Er_2F_{36}N_4O_{16}S_{16}$: C, 30.88; H, 1.40; N, 2.06. Found: C, 31.00; H, 1.52; N, 2.04. Anal. Calcd (%) for $C_{70}H_{38}Yb_2F_{36}N_4O_{16}S_{16}$: C, 30.75; H, 1.39; N, 2.05. Found: C, 30.97; H, 1.44; N, 1.99.

*$[Tb(hfac)_3(\mathbf{L}^2)]_2$ (Ln = Tb (**6**) and Dy (**7**)).* A total of 0.04 mmol of $Ln(hfac)_3{\cdot}2H_2O$ was dissolved in 10 mL of boiling *n*-heptane and then added to a solution of 10 mL of $CHCl_3$ containing 23.0 mg of $\mathbf{L}^2$ (0.04 mmol). After 15 min of stirring, the reaction mixture was slowly evaporated to give orange single crystals which are suitable for X-ray studies. Yield: 80 mg (74%) and 84 mg (77%), respectively, for compounds **6** and **7**. Anal. Calcd (%) for $C_{70}H_{42}Tb_2F_{36}N_4O_{16}S_{16}$: C, 31.00; H, 1.55; N, 2.07. Found: C, 31.21; H, 1.60; N, 2.10. Anal. Calcd (%) for $C_{70}H_{42}Dy_2F_{36}N_4O_{16}S_{16}$: C, 30.94; H, 1.55; N, 2.06. Found: C, 31.07; H, 1.51; N, 2.14.

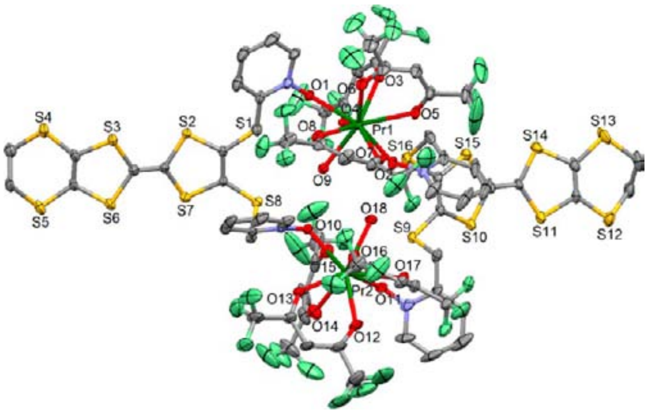

Figure 1. ORTEP view of the dinuclear complex **1**. Thermal ellipsoids are drawn at 30% probability. Hydrogen atoms are omitted for clarity.

Table 2. Selected Bond Lengths (Å) for Complexes 1, 3, 6, and 7

	1	3	6	7
Ln1−O5	2.511(7)	2.338(6)	2.386(5)	2.370(4)
Ln1−O1	2.429(7)	2.298(6)	2.326(4)	2.321(3)
Ln1−O2	2.483(7)	2.329(6)	2.330(5)	2.314(4)
Ln1−O3	2.473(8)	2.380(6)	2.392(5)	2.378(4)
Ln1−O4	2.607(8)	2.325(6)	2.388(5)	2.373(4)
Ln1−O6	2.457(8)	2.423(6)	2.354(5)	2.334(4)
Ln1−O7	2.507(8)	2.388(6)	2.364(6)	2.342(4)
Ln1−O8	2.521(8)	2.362(6)	2.411(5)	2.314(4)
Ln1−O9	2.531(7)	2.347(6)		
Ln2−O10	2.481(7)	2.291(6)		
Ln2−O11	2.439(7)	2.353(7)		
Ln2−O12	2.458(8)	2.382(7)		
Ln2−O13	2.490(7)	2.327(7)		
Ln2−O14	2.465(9)	2.347(6)		
Ln2−O15	2.546(8)	2.403(7)		
Ln2−O16	2.496(8)	2.363(6)		
Ln2−O17	2.532(8)			
Ln2−O18	2.533(7)			

■ RESULTS AND DISCUSSION

Crystal Structure Analysis. *$[Pr_2(hfac)_6(H_2O)_2(\mathbf{L}^1)_2]$ (**1**).* Compound **1** crystallizes in the *Pnaa* (No. 56) orthorhombic space group (Table 1). The asymmetric unit is composed of two $Pr(hfac)_3(H_2O)$ moieties and two $\mathbf{L}^1$ ligands (Figure 1). Each Pr^{III} ion is surrounded by nine oxygen atoms that belong to three $hfac^-$ ligands, one water molecule, and two crystallographically independent monochelating $\mathbf{L}^1$ ligands. The average $Pr{-}O_{L^1}$ distances are shorter (2.46(3) Å) than the average $Pr{-}O_{hfac}$ distances (2.50(4) Å; Table 2) due to the difference of Lewis base character. In any case, the longest distances are observed for $Pr{-}O_{water}$ with an average bond length of 2.532(7) Å. This should be due to the optimization of possible weak hydrogen bonds between both coordinated water molecules (O9···O18 = 3.16(1) Å). The arrangement of the ligands leads to a 4,4,4-tricapped trigonal prism as a coordination polyhedron of the lanthanide ions (D_{3h} symmetry; Figure S1). Such geometry for the Pr^{III} ions is communally observed in molecular structures.[18] The two $Pr(hfac)_3(H_2O)$ moieties are bridged by two $\mathbf{L}^1$ ligands leading to the formation of a dinuclear complex. The intramolecular Pr···Pr distance is equal to 6.407(2) Å. The central C═C bonds of the TTF core are equal to the average value of 1.337(15) Å, attesting to the neutral form of both $\mathbf{L}^1$ ligands. The angle between the planes formed by the TTF cores of the EDT-TTF derivatives is equal to 21.69(7)°. It is worth to notice that the two 2-pyridine-*N*-oxide-methyl-thio arms of $\mathbf{L}^1$ are oriented on the same side of the TTF core. Thus, the $Pr(hfac)_3(H_2O)$ moieties are localized out of the plane formed by the EDT-TTF fragments, which leads to the formation of a dimer of **1** (Figure 2). Each dimer of **1** interacts through short contacts between the ethylenedithio fragment and the 2-pyridine-*N*-oxide ring. These intermolecular

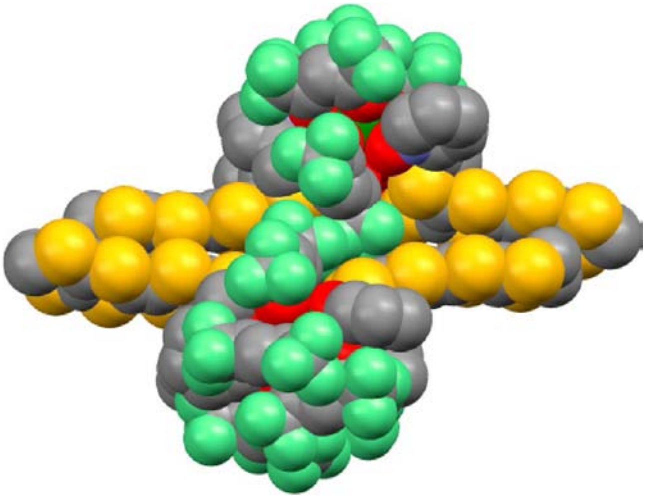

Figure 2. A dimer of complex **1**.

interactions between four dimers results in the formation of a pseudo-cyclic architecture (Figure 3a). Finally, organic (space-filling representation in Figure 3b) and metallo-organic (ball and stick representation in Figure 3b) networks are formed.

*[Ln$_2$(hfac)$_6$($\mathbf{L}^1$)$_2$] (Ln = Tb (**2**), Dy (**3**), Er (**4**), and Yb (**5**)).* All compounds **2**−**5** are isostructural. The full data collection and the refinement of the structure have been done only for **3**, while the cell parameters have been determined for the other remaining derivatives in order to confirm the isomorphism of the four compounds (Table 1).

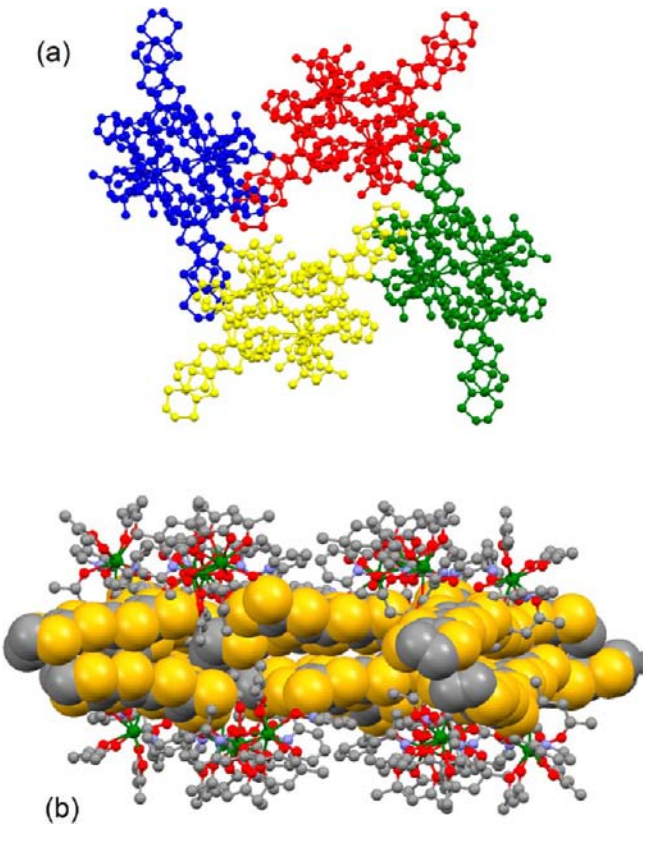

Figure 3. (a) Cyclic architecture formed by the intermolecular interactions between four dimers of **1**. (b) Crystal packing of **1** highlighting the formation of organic (spacefilling) and metallo-organic (ball and stick) networks.

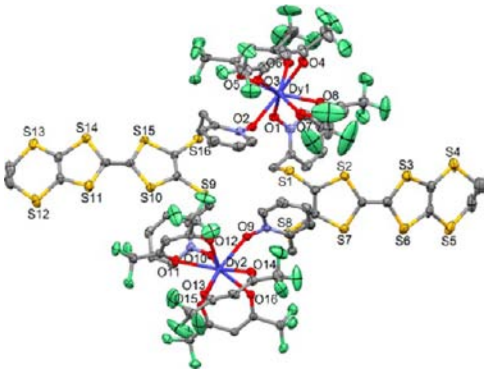

Figure 4. ORTEP view of the dinuclear complex **3**. Thermal ellipsoids are drawn at 30% probability. Hydrogen atoms are omitted for clarity.

Compound **3** crystallizes in the $C2/c$ (No. 15) monoclinic space group (Table 1). The asymmetric unit is composed of two Dy(hfac)$_3$ moieties and two $\mathbf{L}^1$ ligands (Figure 4). Each Dy^{III} ion is surrounded by eight oxygen atoms that belong to three hfac$^-$ ligands and two crystallographically independent monochelating $\mathbf{L}^1$ ligands. The average Dy−O$_L$ distances are shorter (2.31(2) Å) than the average Dy−O$_{hfac}$ distances (2.37(3) Å; Table 2) due to the difference of Lewis base character. The arrangement of the ligands leads to a strongly distorted bicapped square face trigonal prism (C_{2v} symmetry) and a square antiprism (D_{4d} symmetry) as coordination polyhedra for Dy1 and Dy2 lanthanide ions, respectively (Figure S2). The characteristic angles ($\alpha 1$, $\alpha 2$, $\alpha 3$, and $\alpha 4$; Figure S3) for Dy1 are equal to 4.0(2), 19.5(2), 48.0(2), and 40.2(3)° compared to 0, 21.8, 48.2, and 48.2° for a regular bicapped square face trigonal prism.[28] The characteristic angles for Dy2 are equal to 3.4(2), 8.4(3), 49.0(3), and 50.6(3)° compare to 0, 0, 52.4, and 52.4° for a regular square antiprism.[29] The coordination number and the resulting polyhedra in the complexes **2**−**5** are different than in **1** due to the smaller ionic radii of Tb, Dy, Er, and Yb than the one of Pr. The two Dy(hfac)$_3$ moieties are bridged by two $\mathbf{L}^1$ ligands leading to the formation of a dinuclear complex. In **3**, the 2-pyridine-*N*-oxide-methylthio arms occupy both sides of the TTF core, and the intramolecular Dy···Dy distance is equal to 10.054(2) Å, that is much longer than in **1**. The differences of arrangement of $\mathbf{L}^1$, in particular the orientation of the arms, and the possible role of both coordinated water molecules in **1** can explain this observation. The central C═C bonds of the TTF core are equal to the average value of 1.350(15) Å that attests the neutral form of both $\mathbf{L}^1$ ligands. In contrast with **1**, an angle of about 49.33(7)° is measured between the planes formed by the TTF cores of the EDT-TTF derivatives. The crystal packing reveals the formation of a monodimensional organic network along the b axis (Figure 5a) due to S6···S14 contacts (3.373(4) Å) that are shorter than the sum of their van der Waals radii. The organic chains composed of the ligands $\mathbf{L}^1$ are structurally isolated by the perfluorated moieties (Figure 5b). The shortest intermolecular Dy···Dy distance is found to be equal to 8.507(2) Å and shorter than the intramolecular Dy···Dy distance.

$\mathbf{L}^2$·H$_2$O. The ligand $\mathbf{L}^2$ crystallizes in the triclinic $P\bar{1}$ (No. 2) space group (Table 1). The asymmetric unit is composed of one molecule of $\mathbf{L}^2$ and one water molecule (Figure S4). The

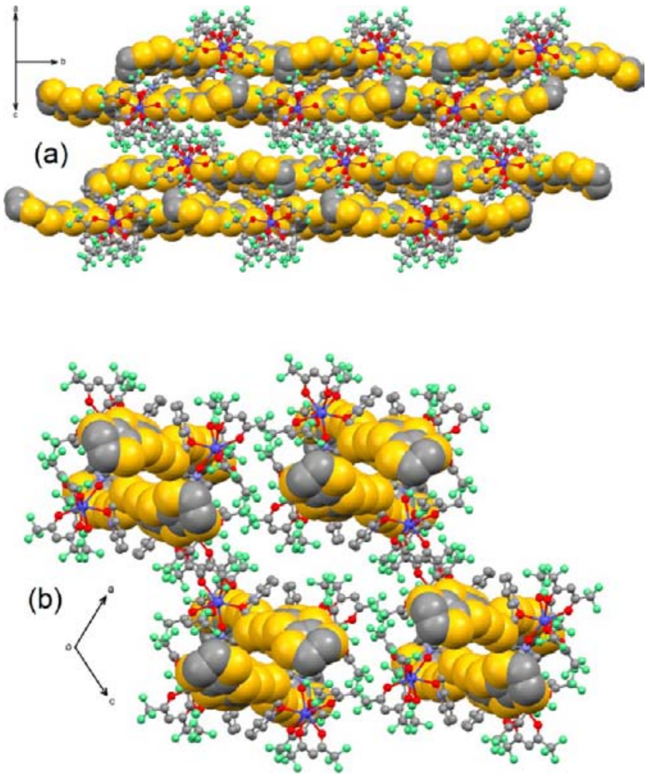

Figure 5. (a) Crystal packing of **3** highlighting the monodimensional organic network along the *b* axis. (b) View in the [101] plane showing the role of the perfluorated ligands in the isolation of the organic chains.

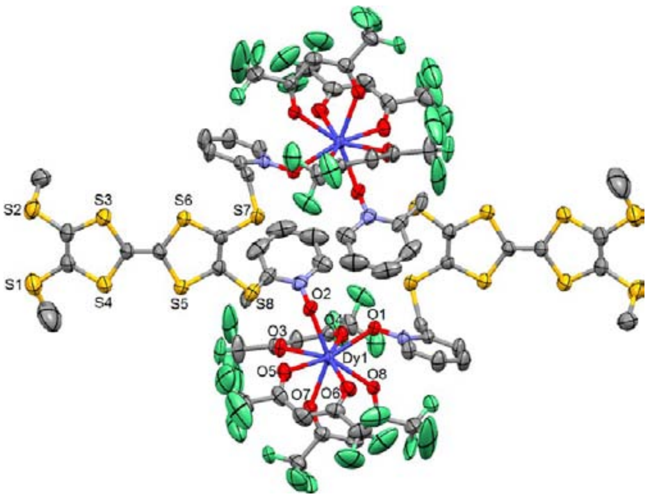

Figure 6. ORTEP view of the dinuclear compound **7**. Thermal ellipsoids are drawn at 30% probability. Hydrogen atoms are omitted for clarity.

central C5–C6 bond length (1.344(4) Å) confirms the neutral form of the ligand. Both 2-pyridine-*N*-oxide-methylthio arms are oriented on the same side compared to the plane formed by the TTF core. The two *N*-oxide have the same orientation, yielding two hydrogen bonds (O1–O3w = 2.995(6) Å and O2–O3w = 2.901(6) Å) with the water molecule (Figure S3). One methyl group is localized in the plane formed by the TTF core, while the second one is oriented on the same side as the two 2-pyridine-*N*-oxide-methylthio arms. The $\mathbf{L}^2$ donors are "head-to-tail" stacked, resulting in dimers with a short S2···S5 contact (3.757(2) Å) and organic columns along the *a* axis (Figure S5). The cohesion between the columns of donors is ensured by the hydrogen bonds network which runs along the *a* axis (Figure S5). The organic columns interact together along the *b* axis through the short S2···S3 contact (3.558(2) Å).

*[Ln(hfac)$_3$($\mathbf{L}^2$)]$_2$ (Ln = Tb (**6**) and Dy (**7**)).* Both compounds are isostructural, and the description is done for **7** while the values for **6** are given between brackets. The series of compounds based on $\mathbf{L}^1$ and $\mathbf{L}^2$ ligands are similar with the formation of dinuclear units in which the two metallic centers are bridged by a donor through the 2-pyridine-*N*-oxide-methylthio arms. Nevertheless, the substitution of the terminal ethylene moieties ($\mathbf{L}^1$) by two methyl groups ($\mathbf{L}^2$) leads to significant structural modifications. Compounds **6** and **7** crystallize in the $P2_1/n$ (No. 14) monoclinic space group (Table 1), and the asymmetric unit is composed of one-half of the dinuclear unit (Figures 6 and S6). Consequently, both Dy [Tb] centers are now crystallographically equivalent. The value of the mean Dy–$\mathrm{O_{hfac}}$ [Tb–$\mathrm{O_{hfac}}$] distances is 2.34(3) [2.38(2)] Å, which is comparable to what is observed in **3** (Table 2). The difference can be attributed to the data collection temperature. The arrangement around the Dy1 [Tb1] ion leads to a strongly distorted coordination polyhedron with characteristic angles of 16.5(2), 22.7(2), 40.2(2), and 38.4(1)° [16.5(2), 22.7(2), 39.8(2), and 38.1(2)°]. In other words, the square face of the polyhedron observed in the $\mathbf{L}^1$-based series ($\alpha 1$) is folded by an angle of 16.5(2)° in the $\mathbf{L}^2$-based series, and consequently the value of the $\alpha 3$ angle decreases to 40.0(2)° (Figure S7). The symmetry of the coordination sphere cannot be any more attributed to a C_{2v} one. The influence of such a change of symmetry on the magnetic properties is studied in the following. The substitution of the ethylene moiety by two methyl groups leads to drastic changes of the intermolecular contacts between the $\mathbf{L}^2$ donors and indirectly in the orientation of the 2-pyridine-*N*-oxide-methylthio arms, which are localized now on the same side of the TTF core. The orientation of the methyl groups and the 2-pyridine-*N*-oxide-methylthio arms are the same in the free $\mathbf{L}^2$ ligand than in the coordination complexes. The $\mathbf{L}^2$ donors are "head-to-tail" stacked to form dimers, and each of these dimers interacts through a S6···S8 short contact (3.829(3) Å) [3.823(4) Å] to form a monodimensional organic network along the *c* axis (Figure 7). The shortest intra- and intermolecular Dy–Dy distances have been found equal to 9.1236(5) [9.1092(7)] Å and 10.4570(3) [10.4723(5)] Å, which is respectively shorter and longer than in **3**. Thus, the dinuclear compound **7** is better isolated than **3** from a magnetic point of view.

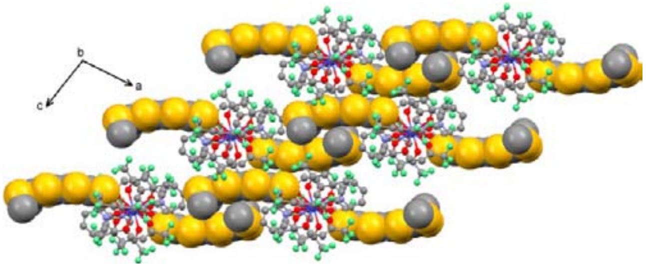

Figure 7. Crystal packing of **7** highlighting the organic (spacefill) and metallo-organic network (ball and stick).

Electrochemical Properties. The redox properties of $\mathbf{L^1}$ and $\mathbf{L^2}$ and the related complexes **1−5** and **6** and **7** are investigated with cyclic voltametry, and the values of the oxidation potentials are listed in Table 3. The cyclic voltamograms show two monoelectronic oxidations at about 0.51 and 0.91 V for $\mathbf{L^1}$ and 0.51 and 0.85 V for $\mathbf{L^2}$, corresponding to the formation of a TTF radical cation and a dication, respectively (Figures S8 and S9). These oxidation potentials are very similar to those found for the BEDT-TTF donor (0.52 and 0.94 V).[30] Upon coordination of the lanthanide, both $E_{1/2}{}^1$ and $E_{1/2}{}^2$ are anodically shifted by 0.02 to 0.05 V compared with the potentials of the free ligands.[3e,31] Complexation to the electron attracting Ln(hfac)$_3$ fragments enhances the electron acceptor effect of the pyridine-*N*-oxide ring, leading to a decrease of the electronic density of the TTF core, and so, positive shifts of $E_{1/2}{}^1$ and $E_{1/2}{}^2$ are observed (Table 3). No duplication of the oxidation waves is observed, signifying that the oxidation and the reduction are simultaneous for the two donors of a complex. The electrochemical properties attest the redox-activity of $\mathbf{L^1}$ and $\mathbf{L^2}$ in the complexes.

Table 3. Oxidation Potentials (V *vs* SCE, nBu$_4$NPF$_6$, 0.1 M in CH$_2$Cl$_2$ at 100 mV.s^{-1}) of the Ligands $\mathbf{L^1}$ and $\mathbf{L^2}$ and Complexes 1−7

	$E_{1/2}{}^1$	$E_{1/2}{}^2$
$\mathbf{L^1}$	0.514	0.907
$\mathbf{L^2}$	0.514	0.847
1	0.544	0.932
2	0.557	0.934
3	0.529	0.933
4	0.535	0.936
5	0.538	0.929
6	0.530	0.894
7	0.513	0.886

Magnetic Properties. *Static Measurements.* The thermal variations of the $\chi_M T$ products for **1−5** are given in Figure 8. All the χ_MT products show a monotonic decrease in the temperature range 300−2 K, taking the values of 2.92 and 0.21 cm^3 K mol^{-1}, 24.37 and 15.91 cm^3 K mol^{-1}, 27.23 and 20.85 cm^3 K mol^{-1}, 22.70 and 10.13 cm^3 K mol^{-1}, and 4.80 and 1.98 cm^3 K mol^{-1}, respectively, at 300 and 2 K for complexes **1−5**. The experimental room temperature values of $\chi_M T$ are in agreement with the theoretical value of 3.20, 23.64, 28.34, 22.93, and 5.14 cm^3 K mol^{-1} expected for two magnetically isolated Pr^{III}, Tb^{III}, Dy^{III}, Er^{III}, and Yb^{III} ions, respectively.[32] As one can expect from the long magnetic pathway and/or metal−metal distances, no significant exchange interactions between the paramagnetic carriers have been observed. The first magnetization curves at 2 K are depicted in Figure S10 and show classic behavior in the field range 0−5 T for magnetically isolated lanthanides such as those involved in complexes **1−5**. The thermal variations of the $\chi_M T$ products for **6** and **7** are given in Figure 9. Both $\chi_M T$ products show a monotonic decrease upon cooling in the temperature range 300−2 K with the values of 24.36 and 17.06 cm^3 K mol^{-1} and 27.15 and 20.56 cm^3 K mol^{-1} at 2 and 300 K for the complexes **6** and **7**, respectively. The room temperature values are in agreement with the theoretical predictions for two magnetically isolated Tb^{III} and Dy^{III} ions. The first magnetization curves at 2 K are given in Figure S11. They are very similar to those of compounds **2** and **3** with, however, a saturation at lower field in **7** compared to **3**.

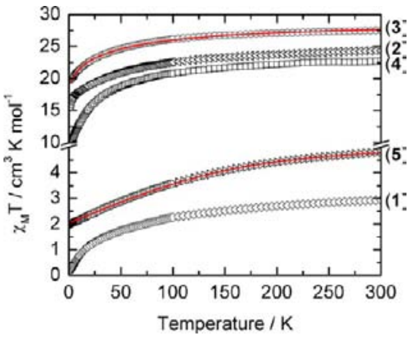

Figure 8. Thermal variation of $\chi_M T$ for **1** (lozenges), **2** (left triangles), **3** (circles), **4** (squares), and **5** (right triangles). The red line corresponds to best fitted curve for compounds **3** and **5** (see text).

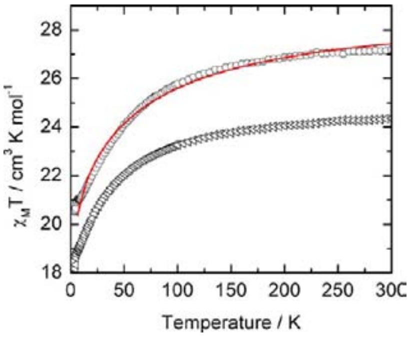

Figure 9. Thermal variation of $\chi_M T$ for **6** (triangles) and **7** (circles) with the best fitted curve (red line) for compound **7** (see text).

Dynamic Measurements. Among the seven investigated compounds, only compound **7** shows a significant out-of-phase component (χ_M'') in a zero dc field (Figure S12) at the lowest temperature (1.8 K). However, the amplitude of χ_M'' corresponds to only few percent (~3%) of the in-phase component at 1000 Hz. The application of a small external dc field dramatically modifies the relaxation process. Indeed, the maximum on the χ_M'' vs ν (ν is the frequency in Hertz of the oscillating ac field) at 1.8 K is shifted to lower frequency on applying external dc field (Figure S13). The optimum field for which the relaxation at a given temperature is the slowest is found around 1200 Oe. The frequency dependence of the ac susceptibility can be analyzed in the framework of the extended Debye model both for field and temperature variations.[33] The striking feature at 1.8 K is that the relaxing fraction of the magnetization $(\chi_T - \chi_S)/\chi_T$ (where χ_T and χ_S represent the adiabatic and the isothermal susceptibilities) increases drastically with the field from 39% at 200 Oe up to 90% at the optimum field. There is one crystallographic Dy site in compound **7**; thus all magnetic moments should relax at the same rate as far as spin−lattice relaxation is concerned. The temperature dependence of the relaxation time at 1200 Oe extracted from the extended Debye model between 1.8 and 4 K is shown in Figure 10 (Table S2). The relaxation time follows the Arrhenius law $\tau = \tau_0 \exp(\Delta/kT)$ only above 3 K with τ_0 = 6.2(5) × 10^{-6} s and Δ = 8.7(2) cm^{-1}. The Cole−Cole plots[33b] normalized to their isothermal value are represented in Figure 11. Clearly, the plots do not collapse on a single master curve,

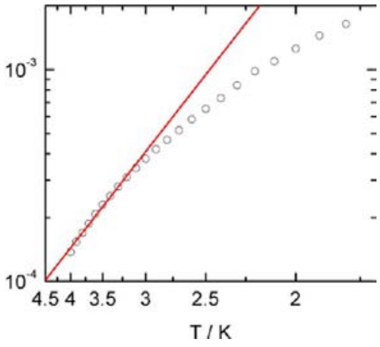

Figure 10. Temperature dependence of the relaxation time of compound **7** measured at 1200 Oe between 1.8 and 4 K. The red line corresponds to the best fit with a Arrhenius law in the range 3−4 K.

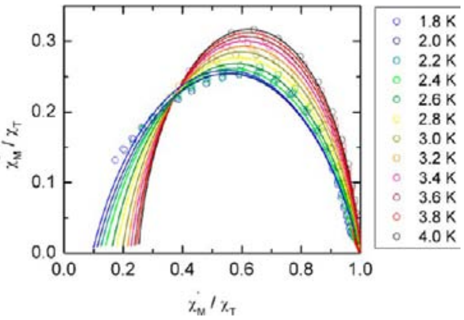

Figure 11. Normalized Cole−Cole plots in the temperature range 1.8−4 K.

and the deviation to the usual flattened semicircle is pronounced at high frequency (left side in Figure 11) and at lower temperature than 3 K. It indicates a deviation from the standard extended Debye model, and it coincides with the temperature at which the relaxation time deviates from the Arrhenius law in Figure 10. Dynamical behavior of the magnetism of compound **7** shows characteristics of a Single Ion Magnet (SIM). In lanthanide based SIMs the barrier height, Δ, is related to the splitting of the M_J states due to the crystal field effects on the $^{2S+1}L_J$ multiplets. In the first approximation, the slowing down of the magnetization reversal occurs when the lowest state corresponds to the highest M_J value (Ising type anisotropy). Δ is then the energy of the levels with the smallest M_J values (0 or ±1/2 for non-Kramers and Kramers ions, respectively). In the equivalent operators model, the crystal field effect, which describes the zero-field splitting, is expressed as polynomials of the total angular momentum matrices (J^2, J_z, J_+, and J_-):

$$\hat{H}_{ZFS} = B_2^0\widehat{\mathbf{O_2^0}} + B_2^2\widehat{\mathbf{O_2^2}} + B_4^0\widehat{\mathbf{O_4^0}} + B_4^2\widehat{\mathbf{O_4^2}} + B_4^4\widehat{\mathbf{O_4^4}} + B_6^0\widehat{\mathbf{O_6^0}} + B_6^2\widehat{\mathbf{O_6^2}} + B_6^4\widehat{\mathbf{O_6^4}} + B_6^6\widehat{\mathbf{O_6^6}}$$

where the $\widehat{\mathbf{O_k^q}}$'s are the operators equivalents and the B_k^q's connected to the crystal field parameters.[34] M_J's are good quantum numbers of $\widehat{\mathbf{O_k^0}}$ (k = 2, 4, 6), while a mixing occurs for $q \neq 0$. In a square antiprism environment (D_{4d}), only the B_k^0 are nonvanishing, while in D_{2d}, B_4^4 and B_6^4 must be added.[35] We attempted to reproduce the temperature dependence of static measurements ($\chi_M T$) for compound **7** and to compare it with the energy barrier from the dynamic measurements. The minimization procedure uses MIGRAD in the MINUIT Fortran program.[36] The minimization procedure converges with five free parameters with the fitted parameters $g_{15/2} = 4/3$ (fixed), $B_2^0 = -0.9594$ cm^{-1}, $B_4^0 = 0.009952$ cm^{-1}, $B_4^4 = -0.0434$ cm^{-1}, $B_6^0 = 9.724 \times 10^{-5}$ cm^{-1}, and $B_6^4 = 7.273 \times 10^{-4}$ cm^{-1} ($R = 1/Npts[(\chi_M T_{exp} - \chi_M T_{calc})^2/\chi_M T_{exp}{}^2]^{1/2} = 8.12 \times 10^{-5}$; Figure 9). With this set of parameters, it is possible to reproduce the field dependence of the magnetization at 2 K. The ground state corresponds to the almost pure $|M_J = \pm 13/2\rangle$ (99%), while the first excited state ($\pm 0.77|\pm 11/2\rangle \pm 0.50|\pm 3/2\rangle \pm 0.39|\pm 5/2\rangle$) is located at 26.9 cm^{-1}. This value should in principle define the energy barrier height, and it must be compared with the value determined from dynamic measurements (Δ = 8.7(2) cm^{-1}). The barriers are on the same order of magnitude but differ significantly. This difference may have several origins: (1) The fitting of the dc magnetization might be overparametrized and might therefore provide poor information concerning energy levels. However, it is highly improbable that energy levels condense to a few wavenumbers like it is suggested from dynamic measurements. (2) The barrier height might be underestimated because additional processes are still operating at the measured field (1200 Oe). Zero-field measurements show that fast processes occur which might be related with the weak mixing of the different M_J states in this low symmetry environment. It must be mentioned that the fitting procedure can be applied to compound **3** in considering that the polyhedron symmetry remains D_{2d}. The best fitted curve is represented in Figure 8 with $g_{15/2} = 4/3$ (fixed), $B_2^0 = -0.6371$ cm^{-1}, $B_4^0 = 0.008360$ cm^{-1}, $B_4^4 = -0.03498$ cm^{-1}, $B_6^0 = 9.274 \times 10^{-5}$ cm^{-1}, and $B_6^4 = 5.706 \times 10^{-4}$ cm^{-1} ($R = 1/Npts[(\chi_M T_{exp} - \chi_M T_{calc})^2/\chi_M T_{exp}{}^2]^{1/2} = 4.1 \times 10^{-5}$). In **3**, the barrier is smaller (19 cm^{-1}) than in **7**, which might explain why we do not observe any slowing down in zero-field down to 1.8 K.

Photophysical Properties. *Absorption Properties.* The UV−visible absorption properties of $\mathbf{L^1}$ have been studied in a $CHCl_3$ solution (Figure 12a). Rationalization by TD-DFT calculations was performed following a computational strategy already used successfully on TTF-based systems.[37] The molecular orbital diagram and UV−visible absorption spectra were determined for $\mathbf{L^1}$ (Figures 12b and 13, Table 4). The experimental absorption curve of $\mathbf{L^1}$ has been deconvoluted into five bands (Figure 12a and Table 4).

The calculated UV−visible absorption spectrum for $\mathbf{L^1}$ well reproduces the experimental curve (Figure 12a and b). The lowest energy band was calculated at the value of 24 976 cm^{-1} (experimental value found at 25 600 cm^{-1}, red Gaussian deconvolution) and attributed to π−π* HOMO → LUMO and HOMO → LUMO+1 TTF to methyl-2-Py-*N*-oxide charge transfers (ILCT; Figures 12a and 13, Table 4). The absorption band centered at 29 100 cm^{-1} (red deconvolution) was calculated at 31 002 cm^{-1} and attributed to ILCT transition HOMO → LUMO+5. The following five absorption bands centered at 31 800 cm^{-1} and 36 100 cm^{-1} (orange Gaussian deconvolution) were calculated at the energy of 31 867 cm^{-1} and 34 470 cm^{-1}. They were mainly attributed to π−π* Intra-Donor excitations (ID) (HOMO → LUMO+6/+7). An ILCT contribution (34470 cm^{-1}) was found for this absorption band (Table 4). Finally, the highest energy absorption band centered at 43 600 cm^{-1} (purple deconvolution) was attributed to Intra-Ligand (IL) transitions. They are mainly described by the HOMO−4 → LUMO+3 (40 956 cm^{-1}), HOMO−3 → LUMO+4 (41 518 cm^{-1}), and HOMO−8 → LUMO (43 783 cm^{-1})

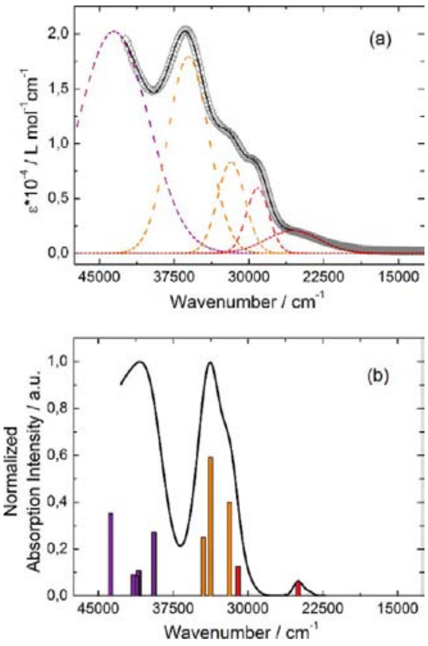

Figure 12. (a) Experimental UV−visible absorption spectra in a $CHCl_3$ solution of $\mathbf{L^1}$ ($C = 4 \times 10^{-5}$ mol L^{-1}; open gray circles). Respective Gaussian deconvolutions (dashed lines) and best fit (full black line; $R = 0.99905$). (b) Theoretical absorption spectra of compounds $\mathbf{L^1}$ (black line). The sticks represent the main contributions of the absorption spectra for $\mathbf{L^1}$.

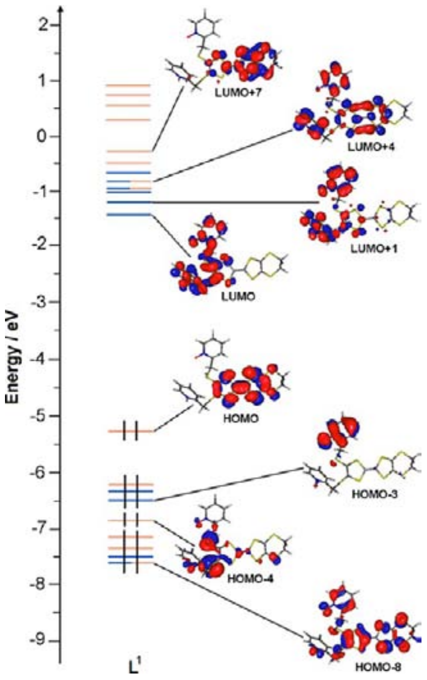

Figure 13. MO diagram of $\mathbf{L^1}$. Energy levels of the centered TTF donor and methyl-2-Py-*N*-oxide acceptor are represented in orange and blue color, respectively.

excitations. The HOMO−8, LUMO+3, and LUMO+4 orbitals are delocalized on the whole ligand (Figure 13).

The UV−visible absorption properties of the coordination complexes **4** and **5** have been first studied in the solid-state (Figures 14a and 15a) and then in $CHCl_3$ solution for **5** (Figure S15a). In all cases, the absorption spectra have been deconvoluted into six bands and are very similar (Table 5). They show a new intense absorption excitation centered at 33 300/33 400 cm^{-1} that corresponds to $\pi-\pi^*$ intrahfac$^-$ excitations.[3e,i] Complexations induce a weak red shift of the ligand-centered ILCT transition due to the Lewis acid behavior of the $Ln(hfac)_3$ moieties enforcing the electron withdrawing character of the 2-pyridine-*N*-oxide fragments even if the electronic communication through the methylthio arms is expected very weak. Thus, the absorption bands are red-shifted to 700 cm^{-1} in coordination complexes compared to those in $\mathbf{L^1}$. Since the shift value is determined from the data in $CHCl_3$ solution, this is a first indication of the stability of the dinuclear complexes in such solvent.

Emission Properties. Emission properties of **4** were measured in the solid state at room temperature (Figure 14b). Upon irradiation at 20 835 cm^{-1} in the lowest-energy absorption band, which was attributed to the HOMO→LUMO ILCT transition, an emission centered at 6660 cm^{-1} (1502 nm) characteristic of the Er^{III} $^4I_{13/2} \rightarrow {}^4I_{15/2}$ transition is observed.[38,3i] No emission centered on the ligand is observed at lower energy, a sign that an efficient energy transfer occurs between the donor excited state and the luminescent state of the Er^{III} ion. Emission properties of **5** were first measured in the solid state at room temperature (Figure S14) and 77 K (Figure 15b), and in $CHCl_3$ solution (Figure S15b). In all cases, the characteristic luminescence profile of Yb^{III} corresponding to the $^2F_{5/2} \rightarrow {}^2F_{7/2}$ transition is observed upon irradiation between 20 and 25 000 cm^{-1} (400−500 nm) without any residual ligand centered emission, indicating as for the Er^{III} derivative an efficient sensitization process. In solution, the signal is clearly observed, proof of the complex stability in $CHCl_3$, but remains broad and poorly resolved. The solid state luminescence spectra are better resolved in particular at low temperatures. Their comparison indicates that at room temperature, additional emission bands at higher energy are displayed at 10 395 cm^{-1} and 10 590 cm^{-1} (Figure S14). These emissions could be assigned to transitions from thermally populated higher crystal-field sublevel of the $^2F_{5/2}$ excited state (+191 cm^{-1} and +386 cm^{-1}).[38] At 77 K, the signal is well resolved (Figure 15b), and four transitions are clearly identified at the energies of 9728 cm^{-1}, 9852 cm^{-1}, 9980 cm^{-1}, and 10 215 cm^{-1} that correspond to the degeneracy of the $^2F_{7/2}$ ground state (Kramer's doublets). The total splitting is determined equal to 487 cm^{-1}. The values of this splitting for a Yb^{III} ion in a distorted and regular[39] D_3 symmetry are 455 cm^{-1} and 372 cm^{-1}, respectively, while a splitting of 528 cm^{-1} is found for a Yb complex in a low symmetry. The value of 487 cm^{-1} seems to correspond to a quite low symmetry that is in agreement with the lowest symmetry of the coordination sphere around the Yb^{III} ions in **4** (distorted bicapped square face trigonal prism). In addition, emission spectroscopy provides a direct probe of the ground state multiplet splitting which can be confronted to magnetic data, with the same model we have used for compound **7**. The best agreement is obtained for $g_{7/2} = 8/7$ (fixed), $B_2^0 = 0.4826$ cm^{-1}, $B_4^0 = 0.316$ cm^{-1}, $B_4^4 = 0.520$ cm^{-1}, $B_6^0 = 2.313 \times 10^{-3}$ $cm^{-1,}$ and $B_6^4 = 6.954 \times 10^{-5}$ cm^{-1} ($R = 1/Npts[(\chi_M T_{exp} - \chi_M T_{calc})^2/\chi_M T_{exp}{}^2]^{1/2} = 1.123 \times 10^{-4}$; Figure 8). The agreement is satisfactory, and the simulated first magnetization curve at 2 K with this set of parameters almost coincides with the experiment (Figure S9). The diagram of energy levels is represented in Figure 16. The energy states correspond almost (99.9%) to pure M_J states, the ground state being $|\pm 5/2\rangle$. The emission spectrum at 77 K can be directly

Table 4. TD-DFT Calculated Excitation Energies and Main Compositions of the Low-Lying Electronic Transitions for L^1[a]

	energy exp (cm^{-1})	energy theo (cm^{-1})	osc.	type	assignment	transition
L^1	25600	24976	0.03	ILCT	$\pi_{TTF} \rightarrow \pi_{Py\text{-}N\text{-}oxide}{}^*$	H→L (49%) H→L+1 (25%)
	29100	31002	0.06	ILCT	$\pi_{TTF} \rightarrow \pi_{Py\text{-}N\text{-}oxide}{}^*$	H→L+5 (33%)
	31800	31867	0.19	ID	$\pi_{TTF} \rightarrow \pi_{TTF}{}^*$	H→L+6/+7 (18/36%)
	36100	33758 + 34470	0.28 + 0.12	ID + ILCT	$\pi_{TTF} \rightarrow \pi_{TTF}{}^*$	H→L+6/+7 (19/11%)H−4→L (14%)H−1→L/+1 (8/23%)
	43600	40956	0.10		$\pi_{TTF} \rightarrow \pi^*_L$	H−4→L+3 (41%)
		41518	0.04	IL	$\pi_{Py\text{-}N\text{-}oxide} \rightarrow \pi^*_L$	H−3→L+4 (43%)
		43783	0.16		$\pi_L \rightarrow \pi^*_{Py\text{-}N\text{-}oxide}$	H−8→L (44%)

[a] In addition, the charge transfer and the pure intramolecular transitions are reported. ID, IL, and H, L represent the intramolecular TTF (donor) or intramolecular transitions involving the whole ligand, the HOMO, and the LUMO, respectively. Therefore, ILCT for Intra-Ligand Charge Transfer. The theoretical values are evaluated at the PCM($CHCl_3$)-PBE0/SVP level of approximation.

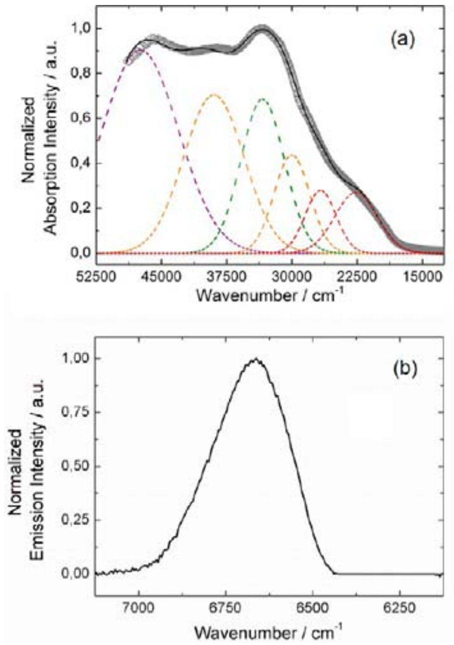

Figure 14. Experimental solid-state absorption and emission for **4** at room temperature. (a) UV−visible absorption spectrum (open circles), respective Gaussian deconvolutions (dashed lines), and best fit (full black line) $R = 0.9990$. (b) Emission spectrum in the near-infrared for $\lambda_{ex} = 20\,835$ cm^{-1} (480 nm).

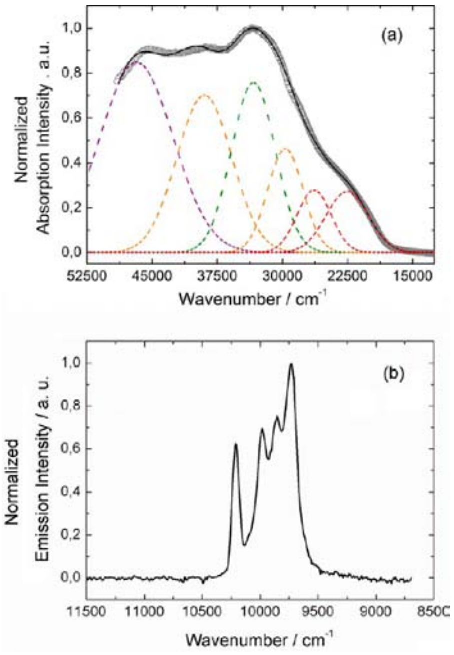

Figure 15. Experimental solid-state absorption and emission for **5**. (a) UV−visible absorption spectrum (open circles), respective Gaussian deconvolutions (dashed lines), and best fit (full black line) $R = 0.9997$. (b) Emission spectrum in the near-infrared for $\lambda_{ex} = 20\,835$ cm^{-1} (480 nm) at 77 K.

compared with the diagram obtained from magnetic measurements.[14h,i] In the Russell−Saunders coupling scheme, the emission spectrum is a picture of the ground state multiplet splitting.[40] The high energy transition corresponds to transition to the ground state and the low energy transition to a transition to the highest excited state of the $^2F_{7/2}$ multiplet. The emission spectrum is also represented in Figure 16. The first excited level corresponding to $M_J = \pm 3/2$ fits exactly (225 cm^{-1}) the second emission line (+234 cm^{-1}), while the last two (405 and 408 cm^{-1}) fall in the middle of the third (+362 cm^{-1}) and fourth (+486 cm^{-1}) lines. The most probable origin of this disagreement is due to the fact that the thermal population at room temperature of such a high energy state is very weak and therefore might not be localized precisely by thermal variation of the magnetic susceptibility. Then, to avoid this problem, we have decided to tackle the determination of the energy levels starting from the energies of the emission lines of the $^2F_{5/2} \rightarrow {}^2F_{7/2}$ transition. To do so, D_{4d} symmetry is considered because only three Stevens operators have to be considered: those with $q = 0$. In this frame, M_J is a good quantum number, and the energy levels can be easily calculated as a function of the three parameters B_2^0, B_4^0, and B_6^0 (see the SI). If one considers that the energy of the emission lines represents a picture of the ground state multiplet splitting, the energy gaps between the

Table 5. Absorption Data for Coordination Complexes 4 and 5

	4 in solid state	**5** in solid state	**5** in $CHCl_3$ solution
experimental energies (cm^{-1})	22600	22500	24900
	26700	26400	29100
	30000	29700	31300
	33400	33300	33900
	39000	39000	37700
	47400	46800	44000

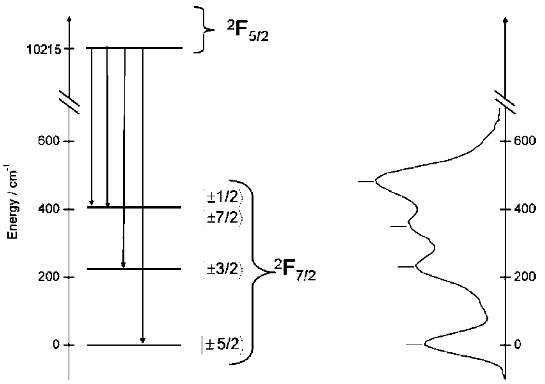

Figure 16. Splitting of the fundamental $^2F_{7/2}$ Yb centered level for compound **5** calculated with parameters in the main text. Labels correspond to the M_J values. On the right, the solid state 77 K emission spectrum is represented with an appropriate shift of the energy scale.

emission lines are a function of B_2^0, B_4^0, and B_6^0 with not less than 24 possible arrangements of the M_J states. Then the system of three equations with three unknowns can be solved. The temperature dependence of $\chi_M T$ can be simulated with these new sets of parameters and compared with the experimental results (Figure S16). First, there is no doubt that the ground state is $M_J = \pm 5/2$ with the first excited state $M_J = \pm 3/2$. Second, the magnetic susceptibility can be reproduced starting from luminescence data in providing a clear view of the constitution (in term of M_J states) of ground state splitting. *In fine*, the combination of magnetism and luminescence provides a fairly good description of the ground state splitting.

■ CONCLUSIONS

Seven dinuclear complexes of the formula $[Ln_2(hfac)_6(H_2O)_x(L^y)_2]$ ($x = 2$ and $y = 1$ for Ln = Pr^{III} (**1**); $x = 0$ and $y = 1$ for Ln = Tb^{III} (**2**), Dy^{III} (**3**), Er^{III} (**4**), and Yb^{III} (**5**); $x = 0$ and y = 2 for Ln = Tb^{III} (**6**) and Dy^{III} (**7**)) have been synthesized. Their X-ray structures reveal that the surroundings of each Ln^{III} center are filled by two *N*-oxide groups coming from two different ligands $\mathbf{L}^y$. The temperature dependences of static measurements for compounds **3**, **5**, and **7** have been fitted considering the Dy^{III} and Yb^{III} in a D_{2d} environment. The ground state corresponds to the almost pure $|M_J = \pm 13/2\rangle$, while the first excited state $(\pm 0.77|\pm 11/2\rangle \pm 0.50|\pm 3/2\rangle \pm 0.39|\pm 5/2\rangle)$ is located at 19 cm^{-1} and 26.9 cm^{-1} for **3** and **7**, respectively. UV−visible absorption has been experimentally measured and rationalized by TD-DFT calculations. Upon irradiation in the range 25 000−20 835 cm^{-1}, both compounds **4** and **5** display a metal-centered luminescence respectively attributed to $^4I_{13/2} \rightarrow {}^4I_{15/2}$ (6660 cm^{-1}) and $^2F_{5/2} \rightarrow {}^2F_{7/2}$ (9972 cm^{-1}) excitations at 77 K and room temperature. Emission spectroscopy provides a direct probe of the ground state multiplet splitting which has been correlated to magnetic data. The ground state being $|\pm 5/2\rangle$ with the first excited level ($M_J = \pm 3/2$) has been calculated at +225 cm^{-1} fitting exactly the second emission line (+234 cm^{-1}). The energy splitting of the M_J states of the $^2F_{7/2}$ ground state have been determined from both the fit of the magnetic data and the energies of the emission lines. While no out-of-phase-signal is detected for **3**, the change of ligand $\mathbf{L}^1$ for $\mathbf{L}^2$ induces a single molecule magnet behavior for **7** which is in agreement with the increase of energy between the ground and first excited states in **7** compared to **3**. The direct correlation between magnetic and optic properties confirms the key roles played by the first excited state in molecular magnetism.

■ ASSOCIATED CONTENT

Ⓢ Supporting Information

Crystallographic information in CIF format, molecular structures of **1** (Figure S1), **3** (Figure S2), and **7** (Figure S7) highlighting the coordination polyhedra; α characteristic angles calculated for Ln1 ion in **2**−**5** compounds (Figure S3); ORTEP view (Figure S4) and crystal packing (Figure S5) of $\mathbf{L^2{\cdot}H_2O}$; ORTEP view for **6** (Figure S6); cyclic voltametry for $\mathbf{L}^1$, $\mathbf{L}^2$, and **1**−**7** (Figure S8 and S9); first magnetization for **1**−**7** (Figures S10 and S11); additional *ac* measurements for **7** (Figures S12 and S13); absorption and emission spectrum for **5** at room temperature (Figures S14 and S15); dc fits for **5** (Figure S16); dynamic parameters for **7** (Tables S1 and S2). This material is available free of charge via the Internet at http://pubs.acs.org.

■ AUTHOR INFORMATION

Corresponding Author

*E-mail: fabrice.pointillart@univ-rennes1.fr.

Notes

The authors declare no competing financial interest.

■ ACKNOWLEDGMENTS

This work was supported by the CNRS, Rennes Métropole, Université de Rennes 1, Région Bretagne and FEDER.

■ REFERENCES

(1) (a) *Conducting and Magnetic Organometallic Molecular Materials*; Fourmigué, M.; Ouahab, L., Eds.; Springer: New York, 2009. (b) *Handbook of Multifunctional Molecular Materials*; Ouahab, L., Ed.; Pan Stanford Publishing: Singapore, 2012 (in press), ISBN 978-981-4364-29-4. (c) Coronado, E.; Galan-Mascaros, J. R.; Gomez-Garcia, C. J.; Laukhin, V. *Nature* **2000**, *408*, 447. (d) Coronado, E.; Day, P. *Chem. Rev.* **2004**, *104*, 5419. (e) Kobayashi, A.; Fujiwara, E.; Kobayashi, H. *Chem. Rev.* **2004**, *104*, 5243 and references therein. (f) Enoki, T.; Miyasaki, A. *Chem. Rev.* **2004**, *104*, 5449. (g) Lorcy, D.; Bellec, N.; Fourmigué, M.; Avarvari, N. *Coord. Chem. Rev.* **2009**, *253*, 1398 and references therein. (h) Pointillart, F.; Golhen, S.; Cador, O.; Ouahab, L. *Dalton Trans.* **2013**, *42*, 1949.

(2) (a) Imakubo, T.; Sawa, H.; Tajima, H.; Kato, R. *Synth. Met.* **1997**, *86*, 2047. (b) Tamura, M.; Matsuzaki, F.; Nishio, Y.; Kajita, K.; Kitazawa, T.; Mori, H.; Tanaka, S. *Synth. Met.* **1999**, *102*, 1716. (c) Dyachenko, O. A.; Kazheva, O. N.; Gritsenko, V. V.; Kushch, N. D. *Synth. Met.* **2001**, *120*, 1017. (d) Otsuka, T.; Cui, H.; Kobayashi, A.; Misaki, Y.; Kobayashi, H. *J. Solid State Chem.* **2002**, *168*, 444. (e) Kushch, N. D.; Kazheva, O. N.; Gritsenko, V. V.; Buravov, L. I.; Van, K. V.; Dyachenko, O. A. *Synth. Met.* **2001**, *123*, 171. (f) Tamura, M.; Yamanaka, K.; Mori, Y.; Nishio, Y.; Kajita, K.; Mori, H.; Tanaka, S.; Yamaura, J. I.; Imakubo, T.; Kato, R.; Misaki, Y.; Tanaka, K. *Synth. Met.* **2001**, *120*, 1041. (g) Pointillart, F.; Maury, O.; Le Gal, Y.; Golhen, S.; Cador, O.; Ouahab, L. *Inorg. Chem.* **2009**, *48*, 7421.

(3) (a) Faulkner, S.; Burton-Pye, B. P.; Khan, T.; Martin, L. R.; Wray, S. D.; Skabara, P. J. *Chem. Commun.* **2002**, *16*, 1668. (b) Pope, S. J. A.; Burton-Pye, B. P.; Berridge, R.; Khan, T.; Skabara, P.; Faulkner, S. *Dalton Trans.* **2006**, 2907. (c) Pointillart, F.; Le Gal, Y.; Golhen, S.; Cador, O.; Ouahab, L. *Chem. Commun.* **2009**, 3777. (d) Pointillart, F.; Le Gal, Y.; Golhen, S.; Cador, O.; Ouahab, L. *Inorg. Chem.* **2009**, *48*, 4631. (e) Pointillart, F.; Cauchy, T.; Maury, O.; Le Gal, Y.; Golhen, S.; Cador, O.; Ouahab, L. *Chem.—Eur. J.* **2010**, *16*, 11926. (f) Pointillart, F.; Le Gal, Y.; Golhen, S.; Cador, O.; Ouahab, L. *Chem.—Eur. J.* **2011**,

17, 10397. (g) Cosquer, G.; Pointillart, F.; Le Gal, Y.; Golhen, S.; Cador, O.; Ouahab, L. *Chem.—Eur. J.* **2011**, *17*, 12502. (h) Pointillart, F.; Klementieva, S.; Kuropatov, V.; Le Gal, Y.; Golhen, S.; Cador, O.; Cherkasov, V.; Ouahab, L. *Chem. Commun.* **2012**, *48*, 714. (i) Pointillart, F.; Bourdolle, A.; Cauchy, T.; Maury, O.; Le Gal, Y.; Golhen, S.; Cador, O.; Ouahab, L. *Inorg. Chem.* **2012**, *51*, 978.

(4) (a) Horrocks De, W. W., Jr.; Bolender, P.; Smith, W. D.; Supkowski, R. M. *J. Am. Chem. Soc.* **1997**, *119*, 5972. (b) De Bettencourt-Dias, A. *Dalton Trans.* **2007**, 2229. (c) Kido, J.; Okamoto, Y. *Chem. Rev.* **2002**, *102*, 2357.

(5) Lempicki, A.; Samelson, H. *Phys. Lett.* **1963**, *4*, 133.

(6) Tang, C. W.; Vanslyka, S. A. *Appl. Phys. Lett.* **1987**, *51*, 2902.

(7) Burroughes, J. H.; Bradley, D. S. C.; Holmes, A. B. *Nature* **1990**, *347*, 539.

(8) Wenzel, T. J. In *Lanthanide Shift Reagents in Stereochemical Analysis*; Morrill, T. C., Ed.; VCH Publishers: Weinheim, Germany, 1986; pp 151−173, Chapter 5.

(9) Hemmila, I. A. *Application of Fluorescence in Immunoassays*; Wiley: New York, 1991.

(10) (a) Faulkner, S.; Matthews, J. L. *Fluorescent Complexes for Biomedical Applications, in Comprehensive Coordination Chemistry*, 2nd ed; Ward, M. D., Ed.; Elsevier: Oxford, 2004' Vol. 9, p 913. (b) Motson, G. R.; Fleming, J. S.; Brooker, S. *Adv. Inorg. Chem.* **2004**, *55*, 361. (c) Bünzli, J.-C. G.; Piguet, C. *Chem. Soc. Rev.* **2005**, *34*, 1048. (d) Zang, F. X.; Hong, Z. R.; Li, W. L.; Li, M. L.; Sun, X. Y. *Appl. Phys. Lett.* **2004**, *84*, 2679. (e) Suzuki, H. *J. Photochem. Photobiol., A* **2004**, *166*, 155. (f) Tanabe, S. *C. R. Chim.* **2002**, *5*, 815. (h) Faulkner, S.; Pope, S. J. A.; Burton-Pye, B. P. *Appl. Spectrosc. Rev.* **2004**, *40*, 1. (g) D'Aléo, A.; Bourdolle, A.; Bulstein, S.; Fauquier, T.; Grichine, A.; Duperray, A.; Baldeck, P. L.; Andraud, C.; Brasselet, S.; Maury, O. *Angew. Chem. In. Ed.* **2012**, *51*, 6622.

(11) Bünzli, J.-C. G.; Piguet, C. *Chem. Rev.* **2002**, *102*, 1897.

(12) Sessoli, R.; Powell, A. K. *Coord. Chem. Rev.* **2009**, *253*, 2328.

(13) (a) Rinehart, J. D.; Fang, M.; Evans, W. J.; Long, J. R. *Nat. Chem.* **2011**, *3*, 538. (b) Rinehart, J. D.; Fang, M.; Evans, W. J.; Long, J. R. *J. Am. Chem. Soc.* **2011**, *133*, 14236. (c) Blagg, R. J.; Tuna, F.; McInnes, E. J. L.; Winpenny, R. E. P. *Chem. Commun.* **2011**, *47*, 10587. (d) Blagg, R. J.; Muryn, C. A.; McInnes, E. J. L.; Tuna, F.; Winpenny, R. E. P. *Angew. Chem., Int. Ed.* **2011**, *50*, 6530.

(14) (a) Ishikawa, N.; Sugita, M.; Ishikawa, T.; Koshihara, S.; Kaizu, Y. *J. Am. Chem. Soc.* **2003**, *125*, 8694. (b) Wang, Y.; Li, X. L.; Wang, T. W.; Song, Y.; You, X. Z. *Inorg. Chem.* **2010**, *49*, 969. (c) Li, D.-P.; Wang, T.-W.; Li, C.-H.; Liu, D.-S.; Li, X.-Z.; You, X.-Z. *Chem. Commun.* **2010**, *46*, 2929. (d) AlDamen, M. A.; Cardona-Serra, S.; Clemente-Juan, J.-M.; Coronado, E.; Gaita-Arino, A.; Marti-Gastaldo, C.; Luis, F.; Montero, O. *Inorg. Chem.* **2009**, *48*, 3467. (e) Jiang, S.-D.; Wang, B.-W.; Su, G.; Wang, Z.-M.; Gao, S. *Angew. Chem., Int. Ed.* **2010**, *49*, 7448. (f) Jeletic, M.; Lin, P.-H.; Le Roy, J. J.; Korobkov, I.; Gorelsky, S. I.; Murugesu, M. *J. Am. Chem. Soc.* **2011**, *133*, 19286. (g) Sessoli, R.; Car, P. E.; Perfetti, M.; Mannini, M.; Favre, A.; Caneschi, A. *Chem. Commun.* **2011**, *47*, 3751. (h) Cuconotta, G.; Perfetti, M.; Luzon, J.; Etienne, M.; Car, P. E.; Caneschi, A.; Calvez, G.; Bernot, K.; Sessoli, R. *Angew. Chem., Int. Ed.* **2012**, *51*, 1606. (i) Long, J.; Vallat, R.; Ferreira, R. A. S.; Carlos, L. D.; Paz, F. A. A.; Guari, Y.; Larionova, J. *Chem. Commun.* **2012**, *48*, 9974. (j) Lin, S. Y.; Wernsdorfer, W.; Ungur, L.; Powell, A. K.; Guo, Y.-N.; Tang, J.; Zhao, L.; Chibotaru, L. F.; Zhang, H. J. *Angew. Chem., Int. Ed.* **2012**, *51*, 12767. (k) Ruiz, J.; Mota, A. J.; Rodriguez-Diéguez, A.; Titos, S.; Herrera, J. M.; Ruiz, E.; Cremades, E.; Costes, J.-P.; Colacio, E. *Chem. Commun.* **2012**, *48*, 7916. (l) Xue, S.; Zhao, L.; Guo, Y.-N.; Chen, X.-H.; Tang, J. *Chem. Commun.* **2012**, 7031. (m) Habib, F.; Long, J.; Lin, P.-H.; Korobkov, I.; Ungur, L.; Wernsdorfer, W.; Chibotaru, L. F.; Murugesu, M. *Chem. Sci.* **2012**, *3*, 2158. (n) Sulway, S. A.; Layfield, R. A.; Tuna, F.; Wernsdorfer, W.; Winpenny, R. E. P. *Chem. Commun.* **2012**, 1508. (o) Guo, F.-S.; Liu, J.-L.; Leng, J.-D.; Meng, Z.-S.; Lin, Z.-J.; Tong, M.-L.; Gao, S.; Ungur, L.; Chibotaru, L. F. *Chem.—Eur. J.* **2011**, *17*, 2458.

(15) (a) AlDamen, M. A.; Clemente-Juan, J. M; Coronado, E.; Marti-Gastaldo, C.; Gaita-Arino, A. *J. Am. Chem. Soc.* **2008**, *130*, 8874. (b) Jiang, S.-D.; Wang, B.-W.; Sun, H.-L.; Wang, Z.-M.; Gao, S. *J. Am. Chem. Soc.* **2011**, *133*, 4730.

(16) (a) Liu, J.-L.; Yuan, K.; Leng, J.-D.; Ungur, L.; Wernsdorfer, W.; Guo, F.-S.; Chibotaru, L. F.; Tong, M.-L. *Inorg. Chem.* **2012**, *51*, 8538. (b) Pointillart, F.; Le Guennic, B.; Maury, O.; Golhen, S.; Cador, O.; Maury, O.; Ouahab, L. *Chem. Commun.* **2013**, *49*, 615.

(17) (a) Rinehart, J. D.; Long, J. R. *Chem. Sci.* **2011**, *2*, 2078. (b) Boulon, M.-E.; Cucinotta, G.; Luzon, J.; Dedl'Innocenti, C.; Perfetti, M.; Bernot, K.; Calvez, G.; Caneschi, A.; Sessoli, R. *Angew. Chem., Int. Ed.* **2013**, *52*, 350.

(18) Richardson, M. F.; Wagner, W. F.; Sands, D. E. *J. Inorg. Nucl. Chem.* **1968**, *30*, 1275.

(19) (a) Spek, A. L. *PLATON*; Utrecht University: Utrecht, The Netherlands, 2005. (b) SHELX97: Sheldrick, G. M. *Acta Crystallogr., Sect. A* **2008**, *64*, 112−122. (c) SIR97: Altomare, A.; Burla, M. C.; Camalli, M.; Cascarano, G. L.; Giacovazzo, C.; Guagliardi, A.; Moliterni, A. G. G.; Polidori, G.; Spagna, R. *J. Appl. Crystallogr.* **1999**, *32*, 115.

(20) Frisch, M. J.; Trucks, G. W.; Schlegel, H. B.; Scuseria, G. E.; Robb, M. A.; Cheeseman, J. R.; Scalmani, G.; Barone, V.; Mennucci, B.; Petersson, G. A.; Nakatsuji, H.; Caricato, M.; Li, X.; Hratchian, H. P.; Izmaylov, A. F.; Bloino, J.; Zheng, G.; Sonnenberg, J. L.; Hada, M.; Ehara, M.; Toyota, K.; Fukuda, R.; Hasegawa, J.; Ishida, M.; Nakajima, T.; Honda, Y.; Kitao, O.; Nakai, H.; Vreven, T.; Montgomery, J. A., Jr.; Peralta, J. E.; Ogliaro, F.; Bearpark, M.; Heyd, J. J.; Brothers, E.; Kudin, K. N.; Staroverov, V. N.; Kobayashi, R.; Normand, J.; Raghavachari, K.; Rendell, A.; Burant, J. C.; Iyengar, S. S.; Tomasi, J.; Cossi, M.; Rega, N.; Millam, J. M.; Klene, M.; Knox, J. E.; Cross, J. B.; Bakken, V.; Adamo, C.; Jaramillo, J.; Gomperts, R.; Stratmann, R. E.; Yazyev, O.; Austin, A. J.; Cammi, R.; Pomelli, C.; Ochterski, J. W.; Martin, R. L.; Morokuma, K.; Zakrzewski, V. G.; Voth, G. A.; Salvador, P.; Dannenberg, J. J.; Dapprich, S.; Daniels, A. D.; Farkas, O.; Foresman, J. B.; Ortiz, J. V.; Cioslowski, J.; Fox, D. J. *Gaussian 09*, revision A.02; Gaussian Inc.: Wallingford, CT, 2009.

(21) (a) Perdew, J. P.; Burke, K.; Ernzerhof, M. *Phys. Rev. Lett.* **1996**, *77*, 3865. (b) Adamo, C.; Barone, V. *J. Chem. Phys.* **1999**, *110*, 6158.

(22) Weigend, F.; Ahlrichs, R. *Phys. Chem. Chem. Phys.* **2005**, *7*, 3297.

(23) Tomasi, J.; Mennucci, B.; Cammi, R. *Chem. Rev.* **2005**, *105*, 2999.

(24) (a) Cossi, M.; Barone, V. *J. Chem. Phys.* **2001**, *115*, 4708. (b) Improta, R.; Barone, V.; Scalmani, G.; Frisch, M. J. *J. Chem. Phys.* **2006**, *125*, 054103.

(25) Allouche, A.-R. *J. Comput. Chem.* **2011**, *32*, 174.

(26) Binet, L.; Fabre, J. M.; Montginoul, C.; Simonsen, K. B.; Becher, J. *J. Chem. Soc., Perkin Trans. 1* **1996**, 783.

(27) Polasek, M.; Sedinova, M.; Kotek, J.; Vander Elst, L.; Muller, N. R.; Hermann, P.; Lukes, I. *Inorg. Chem.* **2009**, *48*, 455.

(28) (a) King, R. B. *J. Am. Chem. Soc.* **1969**, *91*, 7211. (b) Pointillart, F.; Bernot, K. *Eur. J. Inorg. Chem.* **2010**, *6*, 952.

(29) (a) Muetterties, E. L.; Guggenberger, L. J. *J. Am. Chem. Soc.* **1974**, *96*, 1748. (b) Drew, M. G. B. *Coord. Chem. Rev.* **1977**, *24*, 179.

(30) Liu, S.-X.; Dolder, S.; Rusanov, E. B.; Stoeckli-Evans, H.; Decurtins, S. *C. R. Chim.* **2003**, *6*, 657.

(31) Uzelmeier, C. E.; Smucker, B. W.; Reinheimer, E. W.; Shatruk, M.; O'Neal, A. W.; Fourmigué, M.; Dunbar, K. R. *Dalton Trans.* **2006**, 5259.

(32) Kahn, O. *Molecular Magnetism*; VCH: Weinhem, Germany, 1993.

(33) (a) Dekker, C.; Arts, A. F. M.; Wijn, H. W.; van Duyneveldt, A. J.; Mydosh, J. A. *Phys. Rev. B* **1989**, *40*, 11243. (b) Cole, K. S.; Cole, R. H. *J. Chem. Phys.* **1941**, *9*, 341.

(34) (a) Orbach, R. *Proc. Phys. Soc. A* **1961**, *264*, 458. (b) Rudowicz, C. *J. Phys. C: Solid State Phys.* **1985**, *18*, 1415.

(35) Görlder-Walrand, C.; Binnemans, K. *Handb. Phys. Chem. Rare Earths* **1996**, *23*, 121.

(36) James, F. *MINUIT Function Minimization and Error Analysis*, CERN Program Library Version 94.1; CERN: Geneva, Switzerland, 1994.

(37) (a) Cosquer, G.; Pointillart, F.; Le Guennic, B.; Le Gal, Y.; Golhen, S.; Cador, O.; Ouahab, L. *Inorg. Chem.* **2012**, *51*, 8488. (b) Pointillart, F.; Le Guennic, B.; Golhen, S.; Cador, O.; Maury, O.; Ouahab, L. *Inorg. Chem.* **2013**, *52*, 1610.

(38) (a) D'Aléo, A.; Picot, A.; Beeby, A.; Williams, J. A. G.; Le Guennic, B.; Andraud, C.; Maury, O. *Inorg. Chem.* **2008**, *47*, 10258. (b) D'Aléo, A.; Ouahab, L.; Andraud, C.; Pointillart, F.; Maury, O. *Coord. Chem. Rev.* **2012**, *256*, 1604.

(39) Ziessel, R. F.; Ulrich, G.; Charbonnière, L.; Imbert, D.; Scopelliti, R.; Bünzli, J.-C. G. *Eur. J. Chem.* **2006**, *12*, 5060.

(40) Gonçalves Silva, F. R.; Malta, O. L.; Reinhard, C.; Güdel, H. U.; Piguet, C.; Moser, J.-E.; Bünzli, J.-C. G. *J. Phys. Chem. A* **2002**, *106*, 1670.